Brachytherapy 12 (2013) 654−664

BRACHYTHERAPY

Praseodymium-142 microspheres for brachytherapy of nonresectable hepatic tumors

Maria Clara M. Ferreira[1], Tarun K. Podder[2], Karl H. Rasmussen[3], Jae W. Jung[1,*]

[1]*Department of Physics, East Carolina University, Greenville, NC*
[2]*Department of Radiation Oncology, University Hospitals Seidman Cancer Center, Case Western Reserve University, Cleveland, OH*
[3]*Department of Radiation Oncology, East Carolina University, Greenville, NC*

ABSTRACT

PURPOSE: To perform dosimetric study of ^{142}Pr microspheres for the use as a possible choice of radionuclide in microsphere brachytherapy of nonresectable hepatic tumor for faster dose delivery and facilitated dosimetry for quality assurance.

METHODS AND MATERIALS: Dose distributions of ^{142}Pr and ^{90}Y microspheres within hepatic tumors and blood vessels were calculated using MCNPX2.6 Monte Carlo code. The biological effective doses (BEDs) for ^{142}Pr and ^{90}Y microspheres were calculated and compared using the linear-quadratic model.

RESULTS: Dose distributions due to beta particles were similar for both ^{142}Pr and ^{90}Y. Total initial activity required to achieve the same total dose of 150 Gy at 2 cm from the center of the tumor was 0.662 GBq and 0.191 GBq for ^{142}Pr and ^{90}Y, respectively. For α/β ratio equal to 10 Gy, calculated BED values were 301.0 and 194.7 for ^{142}Pr and ^{90}Y, respectively, considering a total physical dose of 150 Gy.

CONCLUSIONS: Total dose delivery and dose distributions for both ^{142}Pr and ^{90}Y within tumors and blood vessels were obtained and compared. Shorter half-life of ^{142}Pr is an advantage, enabling a faster dose delivery. The higher BED found for ^{142}Pr implies potential improvement in the treatment effectiveness. ^{142}Pr showed to be an attractive option for applications in microsphere brachytherapy.

Keywords: Monte Carlo simulation; Praseodymium-142; Microsphere brachytherapy; Hepatic tumors

Introduction

Microsphere brachytherapy has gained an increased importance among cancer treatment modalities and research topics in radiotherapy (1−4). It is a selective internal radiation therapy, in which the target organ or tumor site receives a relevantly higher dose, whereas the surrounding healthy tissue receives a very lower dose compared with other treatment modalities, for example, the external beam radiation therapy. At the present stage, the technique has been used for unresectable hepatic tumors, when standard treatments such as chemotherapy and radiotherapy are not able to treat the malignancy.

The most common type of malignant liver cancer in adults is hepatocellular carcinoma (HCC) (primary) and metastasized colon cancer (secondary). About 80% of the primary liver cancers are HCC. Primary HCC can be classified into two main groups: a primary single tumor that grows and then spreads to other liver sites and multiple primary tumors throughout the liver (usually as a consequence of other ongoing liver cells damage or cirrhosis). The latter is the most common type in the United States, and the frequency of this type of HCC has been increasing throughout Western countries (5). The estimated number of new cases of liver and intrahepatic bile duct cancers in 2013 is 30,640, with estimated 21,670 cases (70.7%) resulting in deaths. Liver cancer is more common in the continents of Africa (especially in sub-Saharan countries) and Asia (predominantly in the Eastern countries) (6).

Several beta emitters, for example, ^{90}Y, ^{153}Sm, ^{188}Re, ^{32}P, ^{166}Ho, and ^{142}Pr, have been studied and their use in

---

Received 1 February 2013; received in revised form 18 June 2013; accepted 21 June 2013.

Financial disclosure/Conflict of interest: The first and corresponding authors acknowledge the support from a Ralph E. Powe Junior Faculty Enhancement Award provided by Oak Ridge Associated Universities.

* Corresponding author. Department of Physics, East Carolina University, 1000 East Fifth Street, Greenville, NC 27858. Tel.: +1-252-414-4338; fax: +1-252-328-6314.

E-mail address: k311jjw@gmail.com (J.W. Jung).

1538-4721/$ - see front matter
http://dx.doi.org/10.1016/j.brachy.2013.06.007

brachytherapy and microsphere brachytherapy has been increasing (7–16). The most popular radioisotope being currently used in microsphere brachytherapy is ^{90}Y. It is available in the form of glass or resin microsphere, under the brand names of SIR-Sphere (Sirtex Medical Limited, North Sydney, NSW, Australia) and TheraSphere (Nordion Inc., Ottawa, ON, Canada). Production of ^{90}Y microspheres is considered challenging and costly (17). Availability and costs are therefore limiting factors for research improvements and clinical widespread use of the technique. Another issue related to the nuclide is the difficulty of appropriate verification of the activity of the microspheres for quality assurance (4). The activity of ^{90}Y microspheres is usually calculated based on the initial activity provided by the vendor, decay constant, and the time elapsed since the sample was produced. Direct verification of the total activity at the treatment site has been challenging because ^{90}Y is primarily a beta minus emitter (^{90}Y additionally undergoes internal pair production, and its branching ratio is $31.867 \pm 0.47 \times 10^{-6}$) (18). This presents an issue in cases where only a given part of the total activity of the microspheres is delivered. Other nuclides have been proposed as a possible choice for brachytherapy such as ^{32}P (19).

The production of several radionuclides, including ^{32}P, ^{90}Y, and ^{142}Pr, can be done by means of neutron activation (NA). This method consists of bombarding the target atoms with a flux of neutrons. The activity reached through NA is proportional to the number of atoms in the sample, the neutron flux in the reactor, the neutron energy, the neutron absorption cross section of the parent, and the time in which the parent target is exposed to the neutron flux. Radionuclides with larger activation cross section reach a higher saturation activity than those with smaller activation cross section. Therefore, smaller cross sections require higher neutron fluence or longer time for activation. For instance, ^{32}P has a smaller thermal neutron absorption cross section of the parent ($\sigma = 0.18$ b) and lower beta maximum energy ($E_{\max} = 1.709$ MeV) compared with ^{90}Y (cross section of the parent $\sigma = 1.28$ b and $E_{\max} = 2.284$ MeV). On the other hand, ^{142}Pr presents a larger neutron absorption cross section of the parent ($\sigma = 11.40$ b including that of a metastable state) and a relatively high maximum beta energy ($E_{\max} = 2.162$ MeV). The larger neutron absorption cross section of the parent for ^{142}Pr compared with ^{90}Y allows more production and allows for activation in low neutron fluence reactors. Some authors also suggested the possibility of activation of ^{142}Pr using cyclotrons (20). In the previous studies, ^{142}Pr glass microspheres and seeds have been proposed for the treatment of arteriovenous malformation and prostate cancer (15, 16).

Another important factor to consider is the biological effective dose (BED) to the hepatic parenchyma and HCC, which varies greatly with the radionuclides used. This dose is related to the dose delivery time by the radionuclide and the rate of growth and repopulation, repair rate, and other biological factors of the tumor or tissue considered (21). Dose delivery time is closely related to the half-life of the radionuclide. Effects of half-life to obtain the maximum efficiency in delivering the total dose (TD) have been discussed in previous studies. Armpilia *et al.* (22) considered biological factors and tumor growth rates applied in the linear-quadratic model for the assessment of BED values. Studies obtained by Armpilia *et al.* suggested that radionuclides with shorter half-life yield more BED. These benefits may not solely derive from the shorter half-life as the BED to normal tissues is also dependent on the dose rate. Therefore, care must be taken to avoid failure of selective delivery (11, 23, 24).

In the present work, ^{142}Pr was studied as a possible choice of radionuclide for microsphere brachytherapy. ^{142}Pr is a beta-emitter radionuclide of rare earth elements. It has a half-life of 19.12 h and undergoes beta decays 96.3% of the time, with maximum beta energy equal to $E_{\beta^-} = 2.162$ MeV, and presents a gamma yield of 3.7%, with energy $E_\gamma = 1.575$ MeV. The gamma component of ^{142}Pr would potentially allow a direct verification of the sample activity, using NaI detectors, and improved control of possible contaminations, using a calibrated survey meter. Based on the physical and radiobiological properties of this radionuclide, ^{142}Pr glass microspheres are proposed and also compared with ^{90}Y glass microspheres. The contribution to the TD and dose distribution due to the beta and gamma emission of ^{142}Pr was studied and compared with that of ^{90}Y. Tumors and blood vessels embolized with ^{142}Pr and ^{90}Y microspheres were modeled and simulated using MCNPX2.6 code. For the first time, dose distributions and dose coverage to a tumor due to both nuclides were simulated and compared. This study aims to evaluate the feasibility of using ^{142}Pr microspheres for microsphere brachytherapy.

Methods and materials

Comparison of ^{90}Y and ^{142}Pr

Convolution techniques are often used for photon and electron dose calculation. These methods are fast and have a good agreement with Monte Carlo (MC) simulations for simple geometries (25). Convolution techniques calculate the TD by convolving the total energy released per unit mass of a dose point kernel (DPK), which is the radial distribution of dose around an isotropic point source in an infinite water medium. DPK is used to calculate the dose delivered by electrons and has no angular information.

Dose rates due to ^{142}Pr and ^{90}Y point sources were calculated using BRAIN-DOSE DPK code (26). The BRAIN-DOSE code is based on SADDE (27) and VARSKIN (28) codes. BRAIN-DOSE code uses the DPK method to integrate the Berger point kernels over the source volume using the scaled point kernels tabulated by Berger (29)

$$B(\rho,E)=\frac{1}{4\pi\delta\rho^2}\int_0^{E_{\max}}\frac{EN(E)}{X_{90}}F\left(\frac{\rho}{X_{90}},E\right)dE,$$

where ρ is the distance between source point and dose point (centimeter); δ is the density of the irradiated medium (assumed to be unity for tissue) (grams per cubic centimeter); $N(E)$ is the probability that a β^- particle is emitted with energy E; X_{90} is the radius (centimeter) of the sphere within which 90% of the beta energy is deposited from a point source in an infinite medium; and F is a function of ρ and the X_{90} and represents the dimensionless scaled absorbed dose distribution.

Dose rates for point sources using both nuclides were calculated using MCNPX2.6 MC code (30). It has been shown that MCNPX2.6 can be used successfully for the calculation of dose distributions for electrons when using integrated TIGER series (ITS) style (DBCN 18 card = 1), and it has been shown to be in agreement with other versions of MCNP code (31, 32). It can be used for calculating several particles, such as neutron, photon, electron, or coupled neutron/photon/electron transport. Secondary radiations such as positrons, K-edge characteristic x-rays, and bremsstrahlung are included in the default modeling of MCNPX2.6. The continuous slowing down model is used for the electron transport simulation (30). This model takes into account several factors, including the energy, total path length, and total stopping power of the electron; the electron collisional stopping power due to collisions between particle and atoms; the electron radioactive stopping power due to the energy losses during interactions with the Coulomb force field of the atoms or bremsstrahlung; statistical variations in the amount of energy lost in each collision or energy straggling; and multiple scattering distributions.

Figure 1 shows the beta spectrum for ^{142}Pr and ^{90}Y (33, 34) used for the MCNPX2.6 simulation input. The geometry of the sources was modeled, and a series of three-dimensional (3D) mesh tallies (finite volumes used as detectors by MCNPX2.6 for the 3D mapping of the energy deposited in the medium) were positioned along the dose tally points. The number of source electron histories (NPS) was chosen so that there was less than 1.5% statistical error for the points of interest, such as the points close to the source delivering high-dose rates. To obtain less than 1.5% of statistical error, it was required to use at least 2.0×10^7 NPS per simulation. The "ITS style" energy-indexing algorithm (DBCN 18 card = 1) was used. The default ESTEP parameter (number of substeps per energy step depends on the material in which the electrons are traveling and ranges from 2 for $Z = 3-15$ for $Z > 90$) was defined in the material card (35).

Several physical and radiobiological aspects, including physical half-life, dose distribution, and BED for ^{142}Pr and ^{90}Y, were also compared in this work. Tables 1 and 2 list the properties of several beta emitters and the composition of ^{142}Pr and ^{90}Y microspheres. ^{142}Pr rare earth aluminosilicate glass microspheres (17) are composed of 15.5% silica, 8.1% aluminum, 44.5% praseodymium, and 32.1% oxygen. During the NA process, three of the ^{142}Pr rare earth aluminosilicate glass components (Si, Al, and Pr) are activated in the reactor. However, ^{28}Al has only 2.24-min half-life, ^{31}Si has 2.62-h half-life with a small yield of gamma rays (0.07%), and the production of ^{143}Pr with 13.57 d half-life is negligibly small during activation and the gamma yield of it is 1.2×10^{-6}.

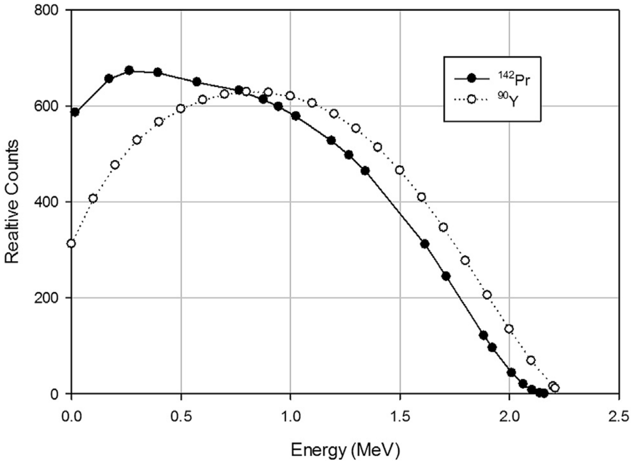

Fig. 1. ^{142}Pr and ^{90}Y beta energy spectrum used for MC simulation (32, 33). MC = Monte Carlo.

Dose rate for ^{90}Y was calculated using DPK method, and the results were compared with the benchmarked calculations from Berger, presented in the previous work from Vynckier and Wambersie (42). The results from DPK calculations were compared with MC results. Dose rates produced by ^{142}Pr and ^{90}Y point sources were also calculated using the DPK method and compared at 0.5 cm away from the point sources.

Dose distribution due to an ensemble of microspheres

MCNPX2.6 code was used to simulate the dose delivered by a given ensemble of an uniformly distributed

Table 1
Physical properties of several beta emitters

Property	^{142}Pr	^{90}Y	^{32}P
Half-life (h)	19.12	64.0	342.7
Maximum beta energy (MeV)	2.162	2.281	1.709
Density of glass (g/cm^3)	4.0	3.29	3.06
Gamma emissions for imaging	Brems[a], 1.58 MeV, γ(3.7%)	Brems[a]	Brems[a]
Thermal neutron cross section	7.5 b (+3.9 b)[b]	1.28 b	0.17 b

[a] Bremsstrahlung.

[b] Cross section of metastable state.

Table 2
Composition of ^{142}Pr and ^{90}Y glass microspheres

Element	^{142}Pr[a]	^{90}Y[b]
Si	0.153	0.194
Al	0.081	0.106
Pr	0.445	0
Y	0	0.303
O	0.321	0.397
Total	1.000	1.000

REAS = rare earth aluminosilicate; YAS = Yttria-Alumina-Silica.

[a] Composition of ^{142}Pr REAS glass (16).

[b] Composition of ^{90}Y YAS glass (55, 56).

microspheres within a tumor for both beta and gamma contributions for ^{142}Pr and for beta contributions for ^{90}Y. A spherical tumor immersed in water was used in this model. The tumor was assumed to be a sphere with 2.5 cm radius or approximately 65 cm^3 in volume as shown in Fig. 2. This value was suggested based on the average reported liver tumors volumes found in the literature (36).

MCNPX2.6 was used to model the geometry of the glass microspheres distributed within the tumor and the different tumor sizes and surrounding water. The source was defined using the source definition (SDEF) parameters in MCNPX2.6. The source geometry had the radioisotope uniformly distributed within the spherical or cylindrical shape. Details of the radionuclide, such as beta energy spectrum, glass density, and percent weight composition, were also entered as parameters for the source definition coding. Number of source electron histories and statistical uncertainties were chosen as the same previously described. 3D mesh tallies were defined as covering the total tumor volume, and extra margin was given to access the dose deposited in the tumor vicinity. Dose rate calculations for the gamma contribution were also performed using MCNPX2.6 simulation. The differences in the code for modeling the gamma component consist of changing the particle type that the MC code will track, from electron (E) to gamma (P), and changing the mash tally distance ranges, because the gamma rays are more penetrating than electrons. The source definitions and geometries used for gamma modeling were the same as used for the electron code.

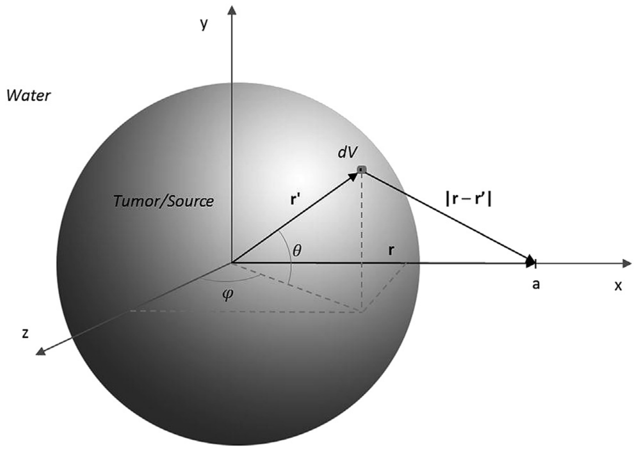

Fig. 2. Geometry used for analytical calculations. Tumor is filled with activated ^{142}Pr microspheres and immersed into the water.

Dose distribution of microspheres within blood vessels for ^{142}Pr and ^{90}Y

A realistic model of microsphere distribution within the liver is proposed in this article. The analysis of post-treated livers has shown that the highest concentration of microspheres is located at the tumor boundaries and blood vessels (37, 38). The microspheres are embolized especially within the tiny blood vessels surrounding the tumor surface, responsible for providing blood supply to the tumor. Dose distribution due to ^{90}Y and ^{142}Pr within modeled blood vessels are simulated using MCNPX2.6 code.

This model uses cylindrical blood vessels with diameters ranging from 25, 50, and 75 μm (diameters based on the average sizes reported by Kennedy *et al.* (37)) and same length as the tumor diameter. Blood vessels were modeled as a cylindrical volume source. The radioisotope was uniformly distributed within the volume sources and located in the center of a 0.2, 0.5, and 1.0 cm radius tumor. Figure 3 shows the modeled blood vessel of 25 μm diameter, both within central tumor and at the periphery of a 0.5 cm tumor radius. A total activity of 8400 and 2500 Bq was used per microsphere of ^{142}Pr and ^{90}Y, respectively. These activities resulted in the same number of disintegrations for both nuclides during the entire treatment period. The same number of disintegrations was chosen to calculate the total physical dose (PD) delivered by each radionuclide for the same number of decays.

The same number of microspheres was considered for both nuclides, that is, 1.2×10^6 microspheres per vial (3). This vial has activity of 3 GBq for TheraSphere. To deliver the same PD, an activity of 10.1 GBq would be required for the ^{142}Pr vial. The gamma component (3.7%) of ^{142}Pr may raise concerns regarding the radiation protection. However, the specific gamma ray dose constant, Γ, for ^{142}Pr (8.050×10^{-6} mSv h^{-1} MBq^{-1}) is considerably smaller than that for the other nuclides used in nuclear medicine and therapy, such as ^{11}C (1.937×10^{-4} mSv h^{-1} MBq^{-1}) and ^{137}Cs (1.032×10^{-4} mSv h^{-1} MBq^{-1}) at 1 m from the source (39). The ambient dose rates for ^{142}Pr were calculated for a point source and compared with the limits for occupational and general public exposures.

The PD distribution for each case was simulated. However, to compare the efficacy of the treatment, the BED should be also taken into account. Therefore, a biological effective dose–volume histogram (40) was plotted for each case studied to access the percent volume of the tumor receiving BED higher than 150 Gy. The commonly used target dose prescribed for microsphere brachytherapy is

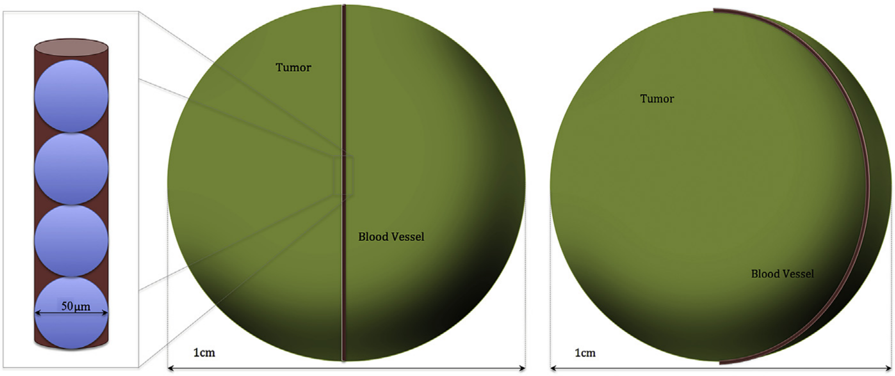

Fig. 3. Modeled blood vessel within and at the periphery of a 0.5 cm tumor radius. Microspheres were embolized within a 25 μm blood vessel.

between 120 and 180 Gy (4); therefore, 150 Gy was chosen to represent the average treatment target dose. In the next section, it will be discussed how to evaluate the BED based on the PD.

Radiological characteristics and production methods for ^{142}Pr and ^{90}Y

The BED values were calculated applying the linear-quadratic model for both ^{142}Pr and ^{90}Y. Considering the relative biological effectiveness (RBE), the BED is regarded as the TD times the relative effectiveness (RE) factor minus biological equivalent of the tumor repopulation (BRF):

$$\mathrm{BED} = (\mathrm{TD})(\mathrm{RE}) - \mathrm{BRF}.$$

The TD is expressed as follows:

$$\mathrm{TD} = \frac{R_0}{\lambda}\left[1 - e^{\left(-\lambda T_{\mathrm{eff}}\right)}\right],$$

where R_0 is the initial dose rate, λ the radionuclide decay constant (per hour), and T_{eff} the effective treatment time (hour), given by

$$T_{\mathrm{eff}} = -\frac{1}{\lambda}\ln\left(\frac{K}{\mathrm{RBE}_{\max}R_0}\right),$$

with K being the tumor repopulation factor (grays per hour), standing for the biological dose required to offset each day's worth of tumor repopulation, given by

$$K = \ln(2)/(\alpha DT)$$

and $\mathrm{RBE}_{\max}$ is the maximum RBE defined as the ratio of linear sensitivity coefficient (α) for high linear energy transfer (LET) test radiation to that for a reference low LET radiation. The RE can be expressed as follows:

$$\mathrm{RE} = \mathrm{RBE}_{\max} + \left[\frac{2R_0\lambda}{(\mu_{\mathrm{tum}} - \lambda)(\alpha/\beta_{\mathrm{tum}})}\right]A(B - C),$$

where A, B, and C are defined as follows

$$A = \frac{1}{1 - \exp\left(-\lambda T_{\mathrm{eff}}\right)},$$

$$B = \frac{1 - \exp\left(-2\lambda T_{\mathrm{eff}}\right)}{2\lambda},$$

$$C = \frac{1 - \exp\left[-T_{\mathrm{eff}}(\mu_{\mathrm{tum}} + \lambda)\right]}{\mu_{\mathrm{tum}} + \lambda},$$

with μ_{tum} being the sublethal damage repair constant (h^{-1}), $(\alpha/\beta)_{\mathrm{tum}}$ the inverse fractionation factor of the tumor (gray), α the linear radiosensitivity coefficient (per gray), and doubling time (DT) the average clonogen DT (h). A numeral software package, Wolfram Mathematica (Wolfram Research Inc., Champaign, IL), was used to perform the BED calculations. BED values for both ^{142}Pr and ^{90}Y given different values of HCC clonogenic DTs were calculated. BED varies with the radionuclide properties, with the tumor radiobiological factors and DT. HCC DTs vary greatly according to the tumor type: well, moderately, or poorly differentiated. The rate of tumor growth can be classified as slow (DT $>$ 100 days), intermediate (50 days $<$ DT $<$ 100 days), or rapid growing tumors (DT $<$ 50 days). The distribution of DT values within each group is positively skewed, with some tumors presenting very long DT values compared with the mean value. For this reason, ranges of values were considered for BED calculation rather than using mean values. DT values for each group were classified as well-differentiated (38–720 days), moderately differentiated (17–380 days), and poorly differentiated HCCs (20–70 days), based on the clinical values obtained in previous studies (41). An α/β value of 10 Gy (tumoral liver) and a total PD of 150 Gy were used for both radionuclides. An α/β value of 2.5 Gy was used for the healthy liver, and a total PD of 10 Gy was used for both radionuclides to calculate the BED for healthy tissues, based on the α/β values previously reported in the literature (23). Total time to deliver 90% of the prescribed dose was estimated for ^{90}Y and ^{142}Pr, by calculating the total time from the microsphere embolization procedure up to the time that only 10% of the initial activity will be remaining in the patient's system. A total PD of 150 Gy was considered for both radionuclides studied to compare the BED. The initial dose rate R_0 was calculated by multiplying the total PD by the radionuclide decay constant (λ), and it can be derived as

$$\mathrm{PD} = \int_0^\infty R_0 e^{-\lambda t} dt = \frac{R_0}{\lambda},$$

$$R_0 = (\mathrm{PD})\lambda.$$

Comparison between the total times to deliver 90% of the prescribed dose was also performed for ^{90}Y and ^{142}Pr.

Source activity and tumor target dose

Source activity for TheraSphere (^{90}Y glass microspheres) was calculated based on the nominal target dose and patients liver mass (3). In this study, a prescription dose of 150 Gy was considered for calculation purposes. The same total PD was considered for ^{142}Pr and ^{90}Y to compare the effects for a fixed dose.

Results

Biological effective dose

The calculated values for BED for both ^{142}Pr and ^{90}Y for the same total PD of 150 Gy are listed in Table 3. For example, for the lowest DT value considered (17 days) or the fastest growing tumor reported in the clinical literature, the BED calculated for ^{90}Y was 104.9 Gy, whereas the BED calculated for ^{142}Pr was 260.0 Gy, representing an increase of 147% of the BED. For the highest DT recorded, 720 days, calculated BED for ^{90}Y was 192.3 Gy, and for ^{142}Pr, it was 299.6 Gy, representing a 56.3% increase in the BED. According to the calculated values of BED, the difference among radionuclides increases as the DT decreases, with the difference being more significant for rapid growing tumors. For the healthy tissue, the calculated BED for a total PD of 10 Gy was 12.0 Gy and 9.02 Gy for ^{142}Pr and ^{90}Y, respectively. The comparison of BEDs for tumor and normal tissue in liver with PD is shown in Fig. 4.

Dose distribution curves for microsphere brachytherapy models

Plots of the calculated DPK for ^{142}Pr and ^{90}Y point sources are shown in Fig. 5. DPK calculation results for ^{90}Y were also compared with the results available in the literature and benchmarked with the experimental data (42). DPK calculations of dose versus distance for ^{90}Y were in close agreement with Berger (42) values for all relevant distances considered in this work. The dose rates obtained using MCNPX2.6 and BRAIN-DOSE were 0.120 mGy/h and 0.119 mGy/h per kBq, respectively, at 0.5 cm away from the source. Dose distributions from BRAIN-DOSE and MCNPX2.6 codes for a ^{142}Pr point source are displayed in Fig. 6. The calculated dose using BRAIN-DOSE code was 4.26% higher than that of MCNPX2.6 code for this given distance. For distances beyond 0.6 cm, MCNPX2.6 presented a higher dose rate than the one observed for BRAIN-DOSE calculations. The differences between these results are because of the fact that MCNPX2.6 accounts for radiation backscatter and multiple electron interactions, as described by the continuous slowing down model. These considerations will increase the dose rate, especially in the range of average or higher energy electrons. BRAIN-DOSE uses the convolution method to calculate the dose, which does not account for energy straggling radiation (24), therefore yielding a lower dose for points away from the source. However, although the differences are large for points beyond 0.6 cm, the dose relative to the TD for these points is very small, for example, at 0.8 cm, MCNPX2.6 calculates 0.0139 cGy/h and BRAIN-DOSE gives 0.0004 cGy/h, representing less than 0.05% of the dose rate at points close to the source.

MCNPX2.6 provided the dose per particle for both beta and gamma for ^{142}Pr and beta contribution for ^{90}Y. Comparison of the total PD along the central axis due to gamma and beta contributions for ^{142}Pr and total PD due to beta contribution for ^{90}Y are presented in Fig. 7. For the results shown in Fig. 7, it was considered a target dose of 150 Gy within the tumor for both nuclides. From the

Table 3
Calculated BED values for a total physical dose of 150 Gy for both ^{142}Pr and ^{90}Y

Tumor type	Well differentiated		Moderately differentiated		Poorly differentiated	
DT (d)	38	720	17	380	20	70
BED (Gy) ^{90}Y	143.4	192.3	104.9	188.5	114.0	162.8
BED (Gy) ^{142}Pr	279.1	299.6	260.0	298.1	264.8	287.7
% Change	95.1	56.3	148	58.1	132	76.7

BED = biological effective dose; DT = doubling time; HCC = hepatocellular carcinoma.

BED calculated for the three ranges of tumor growth or DTs for the different types of HCC. The distribution of DT values for each tumor type is positively skewed; therefore, ranges of values were considered for BED calculation, instead of a mean value. DT ranges for each tumor type were well-differentiated (38–720 days), moderately differentiated (17–380 days), and poorly differentiated HCCs (20–70 days) (41). It is observed that the difference for BED values is more pronounced for rapid growing tumors.

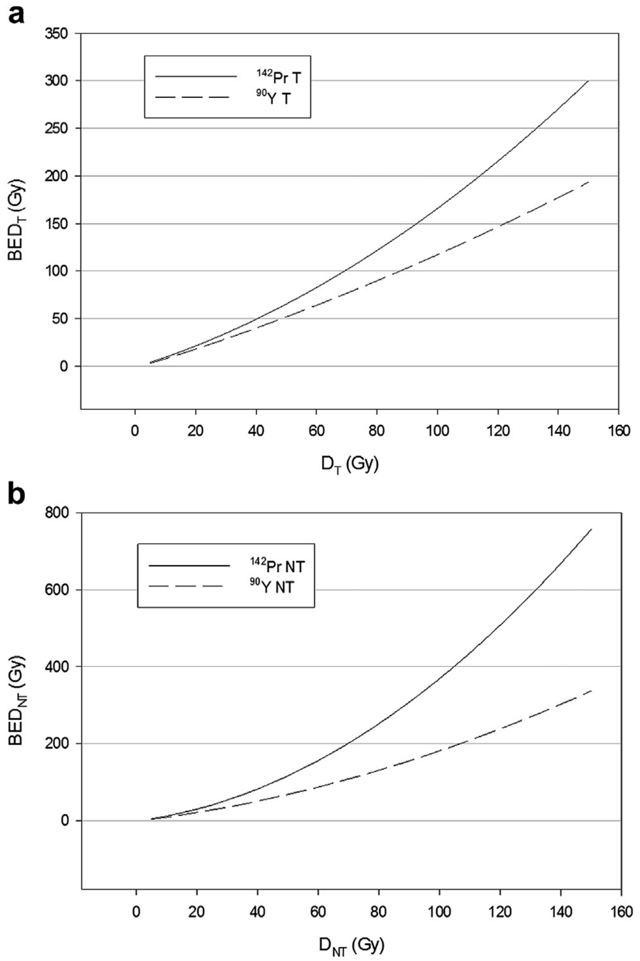

Fig. 4. BED with physical dose for ^{90}Y and ^{142}Pr for (a) tumor (T) and (b) nontumoral tissues (NT). BED = biological effective dose.

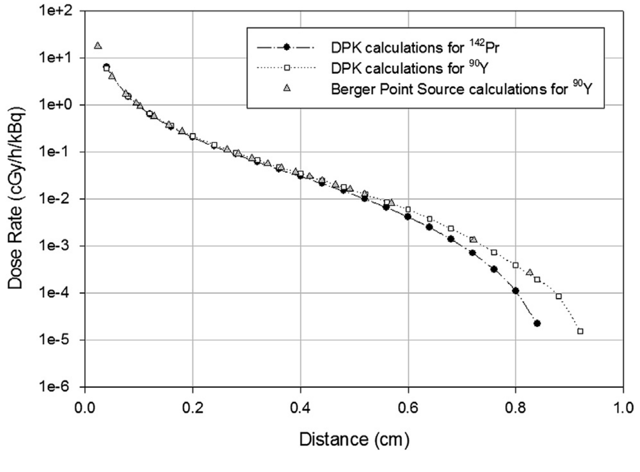

Fig. 5. DPK calculations for 1 kBq ^{90}Y and ^{142}Pr sources and comparison with the benchmarked Berger point source calculations (15) for a 1 kBq ^{90}Y source. DPK = dose point kernel.

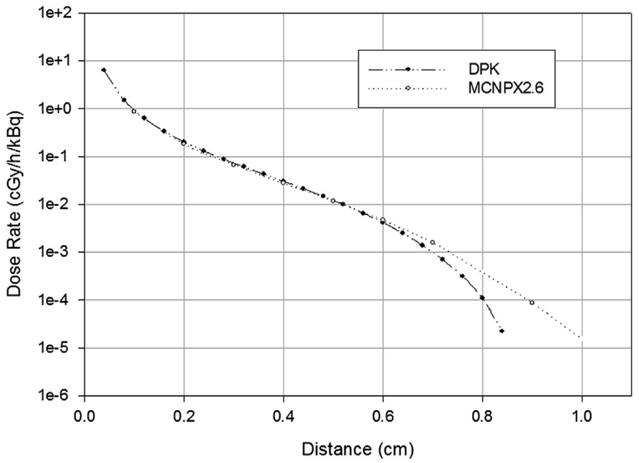

Fig. 6. DPK calculations and MCNPX2.6 simulation of the dose distribution for a 1 kBq ^{142}Pr. A very good agreement is observed between both methods. The increased dose in the tail region for the MCNPX2.6 simulation is because of the fact that DPK calculations does not take into account the dose deposited due to scatter, only due to the primary beta, whereas MCNPX2.6 does. DPK = dose point kernel.

simulation, a beta and gamma dose per decay of 1.95×10^{-12} Gy and 9.77×10^{-15} Gy, respectively, were obtained for ^{142}Pr inside the tumor. A beta dose per decay of 2.36×10^{-12} Gy was obtained for ^{90}Y at the same point. To obtain the desired total PD at the center, a total initial activity of 0.662 and 0.191 GBq was calculated for ^{142}Pr and ^{90}Y, respectively. The beta contribution to the dose drops quickly to zero for points outside the tumor, in this case for points greater than 2.5 cm. Different sizes of spherical tumors were also considered for references of dose distributions inside and in the tumor surroundings. Dose distributions per particle for tumor radii of 1.0, 2.0, 2.5, 3.0, 4.0, and 5.0 cm are displayed in Fig. 8. The total PD distributions near the modeled blood vessels both inside the tumor and at the tumor periphery completely filled with ^{142}Pr are shown in Fig. 9. Total radial dose presented in

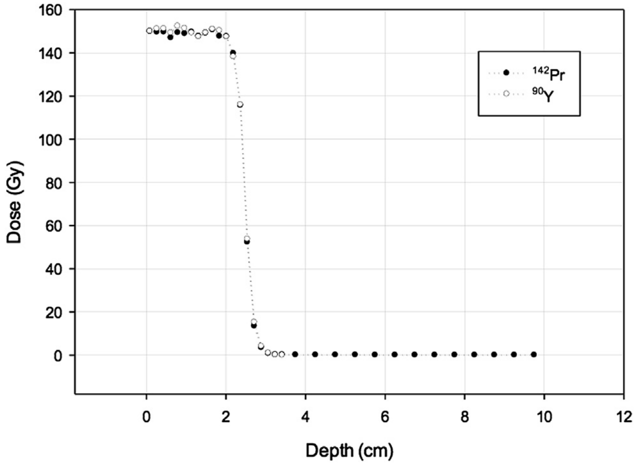

Fig. 7. Central axis view of the beta and gamma contributions to the dose due to ^{142}Pr and beta contribution due to ^{90}Y. Gamma contribution to the total dose for ^{142}Pr cannot be distinguished in the plot because it is about 100 times smaller than the beta dose at the origin.

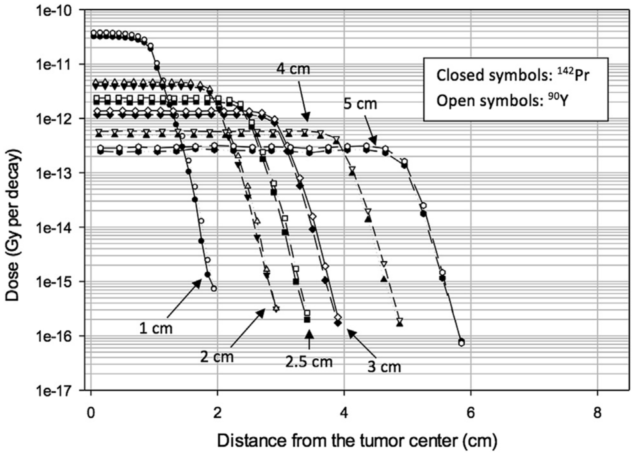

Fig. 8. Tumor radii ranging from 1 to 5 cm. Comparable dose decay curves along the central axis per beta decay for ^{142}Pr (closed symbols) and ^{90}Y (open symbols).

Table 4

Percent of the tumor volume receiving a BED higher than 150 Gy for different tumor radii and blood vessel diameters for both ^{142}Pr and ^{90}Y for a 17-day doubling time

Tumor radius (cm)	Blood vessel diameter[a]					
	25.0 μm		50 μm		75 μm	
	^{142}Pr	^{90}Y	^{142}Pr	^{90}Y	^{142}Pr	^{90}Y
0.2	89.2	60.0	100	100	100	100
0.5	19.9	11.9	40.2	28.6	57.8	44.0
1.0	5.77	4.93	10.7	11.1	15.7	14.0

BED = biological effective dose; BEDVH = biological effective dose–volume histogram.

Values were obtained from the BEDVH analysis for both nuclides.

[a] Diameters were based on average hepatic blood vessel diameter sizes reported in the literature (37).

Fig. 9 was calculated considering the total decays from the entire treatment period of 120 microspheres or 1.0 × 10^{11} decays.

Based on the simulated PD distribution, the biological effective dose–volume histogram distributions for both ^{90}Y and ^{142}Pr were calculated for a TD of 150 Gy. The summary of these findings for all the tumor vessels and tumor sizes studied is listed in Table 4 for tumor DT of 20 days. The initial ambient dose rates due to the ^{142}Pr gamma component calculated for a vial containing 1.2 × 10^6 microspheres that has 10.1 GBq of ^{142}Pr was 0.081 mSv/h. For this vial size and the entire life of this nuclide, the total exposure is calculated to be 2.24 mSv. This calculation was based on conservative assumption that the attenuation from body was not accounted for and the family or caregivers always stayed with the patient at 1 m during the entire treatment period.

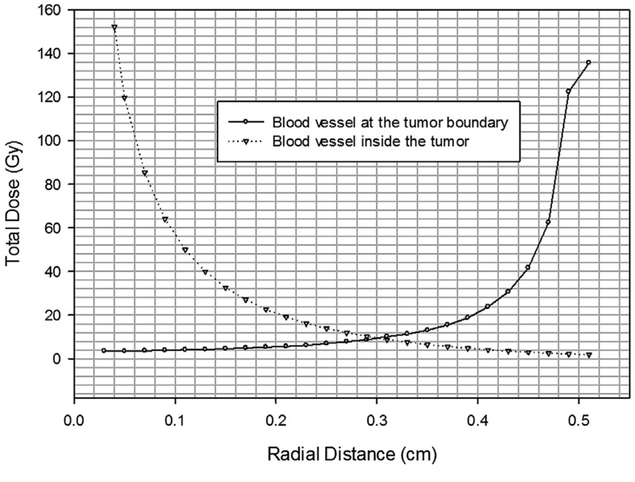

Fig. 9. Total physical dose distribution (gray) generated by the 25 μm radius blood vessel within a 0.5 cm tumor both inside and at the tumor periphery. The dose drops quickly to zero for regions outside the blood vessel, delivering a high dose to the surrounding region.

Discussion

Microsphere brachytherapy for the treatment of hepatic malignancies using ^{142}Pr is an alternative possibility in addition to the currently used radionuclide ^{90}Y, especially for rapid growing tumors with high DTs. ^{142}Pr microspheres can be easily activated in a low neutron flux reactor such as 1 MW TRIGA (Training, Research, Isotopes, and General Atomics) reactor. These TRIGA reactors are usually found in several research centers, making it widely available and possibly reducing total treatment costs for microsphere brachytherapy of the liver because of the proximity of the activation to the treatment site. Gamma-emitting impurities generated during the activation process are expected to be negligible. Therefore, they may not be a concern regarding the additional dose to the patient and staff. However, precaution should be considered during production of microspheres for avoiding additional impurities. This would need to be confirmed via direct measurement of the physical microspheres in the future study.

The time to deliver 90% of the dose (T_{90}) for ^{142}Pr is approximately 30% of T_{90} for ^{90}Y. This is one advantage of using ^{142}Pr over ^{90}Y because of the fact that if the time to deliver the dose decreases, the dose to the normal tissues also decreases from migration (3). A second advantage is that shorter half-lives are preferred because of the higher BED to the HCC. Considering more dose to tumors and irradiation to normal tissues, these ^{142}Pr microspheres would be more efficacious to the patients with lower shunting fractions.

Spatial PD distributions and penetration ranges due to ^{142}Pr were comparable with the ones of the currently used radionuclide ^{90}Y. Point sources as well for an ensemble of microspheres were analyzed, and point source data could be used to access the PD delivered to the patient. Ambient dose rates and TD per a vial were calculated for gamma component (3.7%) of ^{142}Pr to estimate the radiation safety risks presented by this nuclide. Based on the 10 CFR 35 (43), occupational limits (50 mSv) and public limits (5 mSv if infrequent) per year should be observed. Initial ambient dose rates and TD were estimated to be 0.081 mSv/h and 2.24 mSv, respectively, which are below the regulatory exposure limits at 1 m from the source. Radiation levels to the public and staff should be kept as low as reasonably achievable (ALARA). Therefore, additional precaution should be considered such as avoiding proximity with the patient by the caregivers and family within the first few days after treatment.

The models used in this study of ^{142}Pr were based on uniform distribution of activity inside tumors and blood vessels. A truly realistic model would place vessels filled with microspheres through central tumor or at tumor perimeter. Other uniform distribution studies have been proposed in the literature for ^{90}Y dose distribution, for example, partition models, in which the tumor and liver are subdivided into small voxels, containing uniform activities (44). In addition, models using uniform distribution of activities have been used in imaging studies in the attempt to improve the assessment of the dose delivered to the patient (45). Tumor and liver sizes and shapes can vary remarkably from one patient to another (46). For a more detailed dose distribution in a particular patient, a computed tomography (CT) scan of the patient would be necessary, followed by a single-photon emission CT (SPECT) image after dose administration to measure the actual bremsstrahlung distribution. Uniform distribution within voxels for patient-specific dose determination was successfully used by Kennedy *et al.* (37) to describe the dose distribution in the tumor and adjacent organs as liver, kidney, and stomach. The reverse technique, using the ^{142}Pr dose distribution for a point source or a voxel, can be used for treatment planning purposes. This opens possibilities for a future route of this work, possibly starting phantom measurements and animal trials before future clinical trial.

Blood vessels uniformly filled with ^{142}Pr and ^{90}Y microspheres were modeled and simulated using a MC code. Analysis of the dose distribution due to a single embolized blood vessel leads to a more realistic estimation of how microspheres are distributed in the tumor. Characterization of high PD and BED constrained to short distances such as obtained from a single blood vessel may be useful to the current studies being performed on the bystander effect, observed for highly localized doses (47).

Posttreatment biodistribution of the ^{90}Y glass microspheres and dose distribution has been assessed through the detection of bremsstrahlung photons and scarce signal from positron emission (18, 48, 49). The low-energy bremsstrahlung photons are highly scattered in the tissue, leading to a very low signal and consequently a poor spatial resolution of the dose distribution (45). One of the issues with using SPECT for measurement of bremsstrahlung from ^{90}Y is determining directionality (50), which can be improved with the use of pinhole cameras. In the attempt to improve resolution, positron emission tomography (PET) has been proposed in conjunction with CT imaging for the optimization of ^{90}Y processing (50). The range of travel in PET is a limiting factor in the spatial resolution (51). Recently, the administration of a gamma emitter (e.g., ^{177}Lu) concurrent with ^{90}Y has been proposed as an attempt to overcome issues related to the imaging resolution (49). The photon energy spectrum of ^{177}Lu is broad and therefore not being an ideal candidate for imaging (52). The use of ^{166}Ho has been proposed as a possible choice of radionuclide (13, 14). However, ^{166}Ho uses the 81 keV photons for imaging and corrects for the 1.4 MeV photons, which are seen as unwanted scatter degrading the image.

The intrinsic gamma yield of ^{142}Pr allows for potential posttreatment imaging (53). Low-dose-rate monoenergetic photon could be detected using conventional detectors (i.e., NaI scintillation detector) for activity verification before treatment, while delivering a very low dose to the patient. ^{142}Pr could be imaged with 1.58 MeV gamma photons. As the photon signal is strong enough from this isotope, xenon detectors could be used to image the microspheres (54). Using good filtration and septa to reduce the interdetector noise, the 1.58 MeV photon would allow for accurate imaging of the microspheres, with the additional benefit of the strong signal relative to ^{142}Pr after penetrating through the body. The detection of high-energy gamma detection is still challenging because of more Compton scattering and needs further investigation.

Conclusions

Dose distributions were studied for ^{142}Pr and ^{90}Y microspheres for different distributions within a spherical tumor model and cylindrical blood vessel model for the first time in this article. Physical and biological properties of ^{142}Pr and ^{90}Y were also studied and compared. The shorter half-life presented by ^{142}Pr compared with ^{90}Y is a major advantage in the radiobiological tumor response and can also reduce the dose to adjacent organs because of microspheres migration. The shorter half-life implies a higher dose rate, reflected on the higher BED presented by ^{142}Pr. Therefore, these microspheres may be more beneficial than ^{90}Y to the patients with lower shunting fraction. Results for the dose distribution exhibited by ^{90}Y are in agreement with the values reported in the literature. Dose distribution observed for ^{142}Pr was comparable with the dose distribution presented by ^{90}Y. TD contribution due to gamma yield of ^{142}Pr was small and therefore may not be practically significant. This gamma yield, however, could be a potential benefit for biodistribution, dose distribution, and dosimetry assessment. This opens an opportunity for further explorations of the possible imaging capabilities of the gamma yield emitted by ^{142}Pr. ^{142}Pr showed to be an attractive option for applications in microsphere brachytherapy. Future study would include experiment with live animals for simulation validation purposes.

References

[1] Salem R, Thurston KG. Radioembolization with yttrium-90 microspheres: A state-of-the-art brachytherapy treatment for primary and secondary liver malignancies: Part 3: Comprehensive literature review and future direction. *J Vasc Interv Radiol* 2006;17: 1571–1593.

[2] American College of Radiology (ACR) practice guideline for radioembolization with microsphere brachytherapy device (RMBD) for treatment of liver malignancies. 2008. Available at: http://www.acr.org/~/media/D8086059B5F541E9B64E55D68A71693B.pdf. Accessed January 8, 2013.

[3] Kennedy AS, Nag S, Salem R, *et al*. Recommendations for radioembolization of hepatic malignancies using yttrium-90 microsphere brachytherapy: A consensus panel report from the radioembolization brachytherapy oncology consortium. *Int J Radiat Oncol Biol Phys* 2007;68:13–23.

[4] Dezarn WA, Cessna JT, DeWerd LA, *et al*. Recommendations of the American Association of Physicists in Medicine on dosimetry, imaging, and quality assurance procedures for ^{90}Y microsphere brachytherapy in the treatment of hepatic malignancies. *Med Phys* 2011;38:4824–4845.

[5] Hennequin C, Quero L, Rivera S. Radiosensitivity of hepatocellular carcinoma. *Cancer Radiother* 2011;15:39–42.

[6] Cancer facts and figures 2012. American Cancer Society. Available at: http://www.cancer.org/acs/groups/content/@epidemiologysurveillance/documents/document/acspc-031941.pdf Accessed January 8, 2013.

[7] Kennedy AS, Coldwell D, Nutting C, *et al*. Resin ^{90}Y-microsphere brachytherapy for unresectable colorectal liver metastases: Modern USA experience. *Int J Radiat Oncol Biol Phys* 2006;65:412–425.

[8] Sadeghi M, Taghdiri F, Hosseini SH, *et al*. Monte Carlo calculated TG-60 dosimetry parameters for the beta-emitter ^{153}Sm brachytherapy source. *Med Phys* 2010;37:5370–5375.

[9] Fischer M, Kampen WU. Radionuclide therapy of bone metastases. *Breast Care (Basel)* 2012;7:100–107.

[10] Conzone SD, Häfeli UO, Day DE, *et al*. Preparation and properties of radioactive rhenium glass microspheres intended for in vivo radioembolization therapy. *J Biomed Mater Res* 1998;42:617–625.

[11] Oehme L, Kotzerke J. Radiobiological considerations for radioembolization with ^{188}Re-microspheres. *Eur J Nucl Med Mol Imaging* 2009;36:322–325.

[12] Coursey BM, Nath R. Radionuclide therapy. *Phys Today* 2000; 53:25.

[13] Turner JH, Claringbold PG, Klemp PF, *et al*. ^{166}Ho-microsphere liver radiotherapy: A preclinical SPECT dosimetry study in the pig. *Nucl Med Commun* 1994;15:545–553.

[14] Petriev VM, Skvortsov VG, Smakhtin LA, *et al*. Neutron activation preparation of ^{166}Ho-albumin microspheres as a promising radiopharmaceutical for tumor therapy. *Radiochemistry* 2005;47: 301–304.

[15] Lee SW, Reece WD. Dose calculation of ^{142}Pr microspheres as a potential treatment for arteriovenous malformations. *Phys Med Biol* 2005;50:151–166.

[16] Jung JW, Reece WD. Dosimetric characterization of ^{142}Pr glass seeds for brachytherapy. *Appl Rad Isot* 2008;66:441–449.

[17] Hamoudeh M, Kamleh MA, Diab R, *et al*. Radionuclides delivery systems for nuclear imaging and radiotherapy of cancer. *Adv Drug Deliv Rev* 2008;60:1329–1346.

[18] Gates VL, Esmail AA, Marshall K, *et al*. Internal pair production of ^{90}Y permits hepatic localization of microspheres using routine PET: Proof of concept. *Nucl Med* 2011;52:72–76.

[19] Guimaraes CC, Moralles M, Sene FF, *et al*. Dose-rate distribution of ^{32}P-glass microspheres for intra-arterial brachytherapy. *Med Phys* 2010;37:532–539.

[20] Sadeghi M, Bakht MK, Mokhtari L. Practicality of the cyclotron production of radiolanthanide ^{142}Pr: A potential for therapeutic applications and biodistribution studies. *J Radioanal Nucl Chem* 2011;288:937–942.

[21] Hall EJ. *Radiobiology for the radiologist*. Philadelphia, PA: Lippincott; 2000:391–393.

[22] Armpilia CI, Dale RG, Coles IP, *et al*. The determination of radiobiologically optimized half-lives for radionuclides used in permanent brachytherapy implants. *Int J Radiat Oncol Biol Phys* 2003; 55:378–385.

[23] Cremonesi M, Ferrari M, Bartolomei M, *et al*. Radioembolisation with (90)Y-microspheres: Dosimetric and radiobiological investigation for multi-cycle treatment. *Eur J Nucl Med Mol Imaging* 2008; 35:2088–2096.

[24] Dale RG. Dose-rate effects in targeted radiotherapy. *Phys Med Biol* 1996;41:1871–1884.

[25] Mainegra-Hing E, Rogers DWO, Kawrakow I. Calculation of photon energy deposition kernels and electron dose point kernels in water. *Med Phys* 2005;32:685–699.

[26] Dauffy L. Calculation of dose to soft tissue from implanted beta sources [M.S. thesis]. Texas A&M University; 1998.

[27] USNRC. *SADDE (Scaled Absorbed Dose Distribution Evaluator): a code to generate input for VARSKIN*. Washington, DC: United States Nuclear Regulatory Commission; 1989. NUREG/CR-5276.

[28] USNRC. *Dose calculation for contamination of the skin using the computer code VARSKIN*. Washington, DC: United States Nuclear Regulatory Commission; 1987. NUREG/CR-4418.

[29] Berger MJ. Distribution of absorbed dose around point sources of electrons and beta particles in water and other media. *J Nucl Med* 1971;5:5–23.

[30] Pelowitz DB. *MCNPX^{TM} user's manual version 2.6.0*. Los Alamos, NM: Los Alamos National Laboratory; 2008.

[31] Nedaie HA, Mosleh-Shirazi MA, Gharaati H, *et al*. Assessment of different MCNP Monte Carlo codes in electron absorbed dose. *Rep Prac Onc Radiother* 2006;11:293–298.

[32] Schaart DR, Bos AJ, Winkelman AJ, *et al*. The radial depth-dose distribution of a ^{188}W/^{188}Re beta line source measured with novel, ultra-thin TLDs in a PMMA phantom: Comparison with Monte Carlo simulations. *Phys Med Biol* 2002;47:3605–3627.

[33] Jung JW. ^{142}Pr glass seeds for the brachytherapy of prostate cancer [Ph.D. thesis]. Texas A&M University; 2007. ISBN 978-05-491-0565-7.

[34] Cross WG, Ing H, Freedman N. A short atlas of beta-ray spectra. *Phys Med Biol* 1983;28:1251.

[35] Reynaert N, Palmans H, Thierens H, *et al*. Parameter dependence of the MCNP electron transport in determining dose distributions. *Med Phys* 2002;29:2446–2454.

[36] Sarfaraz M, Kennedy AS, Lodge MA, *et al*. Radiation absorbed dose distribution in a patient treated with yttrium-90 microspheres for hepatocellular carcinoma. *Med Phys* 2004;31:2449–2453.

[37] Kennedy AS, Nutting C, Coldwell D, *et al*. Pathologic response and microdosimetry of ^{90}Y microspheres in man: Review of four explanted whole livers. *Int J Radiat Oncol Biol Phys* 2004;60:1552–1563.

[38] Fox RA, Klemp PF, Egan G, *et al*. Dose distribution following selective internal radiation therapy. *Int J Radiat Oncol Biol Phys* 1991;21:463–467.

[39] Unger LM, Trubey DK. *Specific gamma-ray dose constants for nuclides important to dosimetry and radiological assessment*. ORNL/RSIC-45. Oak Ridge National Laboratory; 1982.

[40] Gagne NL, Leonard KL, Huber KE, *et al*. BEDVH-A method for evaluating biologically effective dose volume histograms: Application to eye plaque brachytherapy implants. *Med Phys* 2012;39: 976–983.

[41] Mehrara E, Forssell-Aronsson E, Ahlman H, *et al*. Specific growth rate versus doubling time for quantitative characterization of tumor growth rate. *Cancer Res* 2007;67:3970–3975.

[42] Vynckier S, Wambersie A. Dosimetry of beta sources in radiotherapy I. The beta point source dose function. *Phys Med Biol* 1982;27:1339–1347.

[43] USNRC. *Medical uses of byproduct material. Title 10 code of federal regulations, part 35. United States Nuclear Regulatory Commission*. Washington, D.C.: U.S. Government Printing Office; 2008.

[44] Ho S, Lau WY, Leung TWT, *et al*. Partition model for estimating radiation doses from yttrium-90 microspheres in treating hepatic tumours. *Eur J Nucl Med* 1996;23:947–952.

[45] Rong X, Du Y, Frey EC, *et al*. Development and evaluation of an improved quantitative ^{90}Y bremsstrahlung SPECT method. *Med Phys* 2012;39:2346–2358.

[46] Sarfaraz M, Kennedy AS, Cao ZJ, *et al*. Physical aspects of yttrium-90 microsphere therapy for nonresectable hepatic tumors. *Med Phys* 2003;30:199–203.

[47] Dewhirst M, Fontanella A, Palmer G, *et al*. Vascular response to microbeam radiation therapy *in vivo* using a murine window chamber tumor model. *Med Phys* 2012;39:3983.

[48] Rault E, Staelens S, Van Holen R, *et al*. Fast simulation of yttrium-90 bremsstrahlung photons with GATE. *Med Phys* 2010;37: 2943–2950.

[49] Poorbaygi H, Aghamiri SMR, Sheibani S, *et al*. Production of glass microspheres comprising (90)Y and (177)Lu for treating of hepatic tumors with SPECT imaging capabilities. *Appl Rad Isot* 2011;69: 1407–1414.

[50] Rahmim A, Zaidi H. PET versus SPECT: Strengths, limitations and challenges. *Nucl Med Commun* 2008;29:193–207.

[51] Hsiang KY, Jeffrey S, Jianhua Y, *et al*. *Optimization of yttrium-90 processing on a clinical PET/CT system*. Valencia, Spain: IEEE Nuclear Science Symposium; 2011.

[52] Beauregard JM, Hofman MS, Pereira JM, *et al*. Quantitative ^{177}Lu SPECT (QSPECT) imaging using a commercially available SPECT/CT system. *Cancer Imaging* 2011;11:56–66.

[53] Pelletier CD, Jung JW. *Study of imaging ^{142}Pr microspheres using the gamma emission spectrum in a clinical setting*. Anaheim, CA: IEEE Nuclear Science Symposium; 2012.

[54] Keller H, Glass M, Hinderer R, *et al*. Monte Carlo study of a highly efficient gas ionization detector for megavoltage imaging and image-guided radiotherapy. *Med Phys* 2002;29:165–175.

[55] Erbe EM, Day DE. Chemical durability of Y_2O_3-Al_2O_3-SiO_2 glasses for the in vivo delivery of beta radiation. *J Biomed Mater Res* 1993;27:1301–1308.

[56] Hyatt MJ, Day DE. Glass properties in the yttria-alumina-silica system. *J Am Ceram Soc* 1987;70:283–287.